Intrinsic noise of the single-electron box

Laurence Cochrane[1,2,*] Ashwin A. Seshia[1] and M. Fernando Gonzalez-Zalba[2]

[1]*Nanoscience Centre, Department of Engineering, University of Cambridge, Cambridge CB3 0FF, United Kingdom*

[2]*Quantum Motion, 9 Sterling Way, London N7 9HJ, United Kingdom*

The radio-frequency (rf) single-electron box is becoming an attractive charge sensor for semiconductor-based quantum computing devices due to its high sensitivity and small footprint, which facilitate the design of highly connected qubit architectures. However, an understanding of its ultimate sensitivity is missing due to the lack of a noise model. Here, we quantify the intrinsic noise of the single-electron box arising from stochastic cyclic electron tunneling between a quantum dot and a reservoir driven by a periodic gate voltage. We use both a master-equation formalism and Markov Monte Carlo simulations to calculate the gate-noise current and find that the noise mechanism can be represented as a cyclostationary process. We consider the implications of this cyclostationary noise on the ultimate sensitivity of single-electron box sensors for fast high-fidelity readout of spin qubits, in particular evaluating results for rf reflectometry implementations and the back action of the sensor on a qubit. Furthermore, we determine the conditions under which the intrinsic noise limit could be measured experimentally and techniques by which the noise can be suppressed to enhance qubit-readout fidelity.

I. INTRODUCTION

Semiconductor-based quantum computing architectures are emerging as promising candidates for large-scale quantum information processing [1]. They offer prospects to leverage industrial fabrication techniques [2,3] and to be integrated with classical electronics [4] to scale up current demonstrations of few-qubit processors [5,6]. Fast high-fidelity qubit readout is a critical capability for fault-tolerant operation [7], which in state-of-the-art implementations is provided by charge sensors such as the single-electron transistor (SET) [8–10] probed using radio-frequency (rf) reflectometry techniques [11,12]. Recently, the single-electron box (SEB) [13–15], a single-gate quantum dot (QD) coupled to a single reservoir and driven to periodically vary the QD-reservoir energy detuning [Fig. 1(a)], has attracted increased attention as an alternative sensor to the SET. Demonstrations have achieved comparable readout fidelities to the SET while promising greater scalability and architectural flexibility due to the reduced footprint and electrode count of the SEB [16].

The intrinsic noise of such single-electron devices, arising from the stochastic nature of electron tunneling, determines their ultimate sensitivity and as such deserves close attention. In the case of the SET, its shot noise has been well studied using classical "orthodox" theory [17] and, for low excitation frequencies $\omega_0 \ll 2\pi \langle I \rangle /e$, is governed by the well-known Schottky formula for the current noise spectral density, $S_I = 2eF\langle I \rangle$, where e is the electronic charge, $\langle I \rangle$ is the average current flowing through the device, and the Fano factor F quantifies the correlation between tunneling events. This expression, derived using a master-equation approach [17] and supported by both Markov Monte Carlo (MMC) simulations [18] and experimental measurements [19], has been applied to analyze the ultimate sensitivity of the rf SET [20–22] and its measurement back action [23]. Recently, rf-SET-based single-shot spin readout has approached the theoretical shot-noise limit to within an order of magnitude [24], with further improvements expected by using quantum limited parametric amplification. In the case of the SEB, however, a description of its intrinsic noise limit, analogous to that known for the SET, is lacking.

Previous theoretical and experimental studies of the noise associated with cyclic electron tunneling in the SEB, including investigations of mesoscopic statistical mechanics [25] and quantum thermodynamics [26,27], have focused on the limit of quasiadiabatic driving conditions. However, as we shall demonstrate, the high-frequency

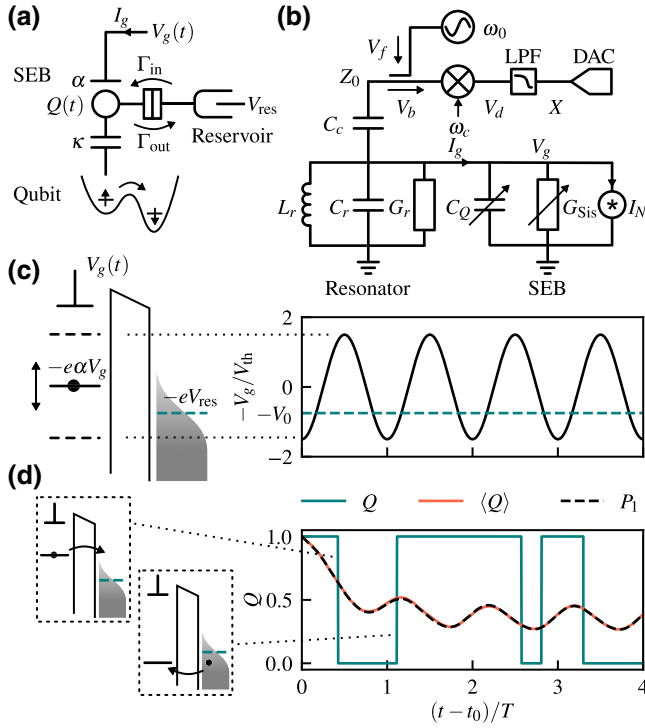---

*Contact author: olc22@cam.ac.uk

FIG. 1. (a) A schematic of the single-electron box (SEB) used as a charge sensor capacitively coupled to a spin qubit; spin-to-charge conversion can be realized by Pauli spin blockade in a double quantum dot (as shown) or spin-selective tunneling to a reservoir. (b) The small-signal equivalent-circuit representation of the SEB embedded in a generalized rf reflectometry setup with a capacitively coupled parallel LC resonator and synchronous demodulation. (c) The periodic gate-excitation signal and (d) the corresponding SEB charge response for an initial dot occupation condition $Q(t_0) = 1$: an instance of the stochastic process $Q(t)$ generated by Monte Carlo simulation (solid green); the ensemble expectation $\langle Q(t) \rangle$ calculated from the mean of 10^4 simulated traces (solid orange); and the solution $P_1(t, t_0)$ to the master equation (dashed black). The energy diagram in (c) illustrates the periodic driving of the dot level with respect to the reservoir Fermi energy. In (d), the energy diagrams show the discrete tunneling-in and -out events that constitute the stochastic $Q(t)$ time trace.

emitters [29]. The experimental dependence of the noise power on the electron-tunneling rate Γ_0 and excitation frequency ω_0 can be well modeled by both a conceptually simple semiclassical model [28] and a more complete account using Floquet scattering theory [30], with simulations based on a tight-binding-chain model [31] supporting this understanding.

However, as we shall show, the time-averaged noise alone is insufficient to characterize the SEB, since correlations in the time-varying noise spectrum can have a significant effect on the signal-to-noise ratio (SNR) after synchronous demodulation. To quantify these correlations, we use the Fourier components $S_I^{n\omega_0}(\omega) = \int S_I(t, \omega) e^{-jn\omega_0 t} dt$ of the periodically varying $S_I(t, \omega)$, which we call "spectral correlation functions," following the nomenclature associated with cyclostationary processes [32]. We note that in the context of single-electron emitters, these spectral correlations have been termed "noise harmonics" [33] or "photon-induced noise" [34] and have been used to investigate signatures of the underlying dynamics of single-electron emitters.

More particularly, in this paper, we present an analysis of stochastic tunneling in the SEB under periodic excitation and provide results relevant to the practical implementation of high-fidelity spin-qubit readout using rf reflectometry. We use a semiclassical master-equation approach to represent periodically driven tunneling as a cyclostationary process [32] and complete the small-signal equivalent-circuit representation of the SEB (consisting of quantum capacitance and Sisyphus resistance [35]) with a noise-current generator I_N [Fig. 1(b)]. We support our analytical expressions for the noise spectrum with Monte Carlo simulations of the underlying time-inhomogeneous Markov process. We study the intrinsic noise spectral density as a function of the SEB parameters and driving conditions and quantify the base-band noise in rf reflectometry readout and the back action induced by the SEB on a nearby qubit. We demonstrate that correlations in the noise spectrum lead to noise enhancement or suppression that depends on the demodulation quadrature, a signature of the intrinsic noise of the SEB that can be experimentally verified and used to optimize readout fidelities.

II. SEB OPERATION AND GATE-NOISE CURRENT

The SEB consists of a driven gate-controlled semiconductor QD coupled via a tunnel barrier to a reservoir [Fig. 1(a)]. When embedded in a resonant circuit [Fig. 1(b)], it modulates the resonant frequency and quality factor through its small-signal gate admittance; this can be inferred from changes in the complex rf reflection coefficient, a scheme termed rf reflectometry [12]. The gate admittance is highly sensitive to the alignment of the QD electrochemical level with the reservoir Fermi level. At

excitation used in rf reflectometry results in a current noise spectral density that is itself a periodic function of time $S_I(t, \omega)$, a property that must be taken into account for an accurate evaluation of the readout sensitivity.

An approach to quantify $S_I(t, \omega)$ can be found in studies of the accuracy of single-electron emitters used as ultraprecise current sources [28–30], such as a mesoscopic capacitor excited by a high-frequency square wave to produce a quantized current. Experimental measurements of the time-averaged noise spectrum $S_I^0(\omega) = \overline{\langle S_I(t, \omega) \rangle}^t$ can demonstrate the accuracy of the source in emitting exactly one electron per cycle, analogous to interferometric methods used in the characterization of single-photon

a large level detuning, Coulomb blockade [9] prohibits electron tunneling, resulting in zero gate admittance; conversely, alignment of the levels permits a cyclic tunneling current to flow and manifests as a maximum in the gate admittance at the corresponding gate voltage.

The sensitivity of the SEB to level misalignment can be utilized for precise charge sensing of nanostructures placed in close proximity and capacitively coupled to the QD of the SEB. In particular, the SEB has been put to use in spin-qubit readout, by combining its sensitive charge sensing capabilities with spin-to-charge conversion techniques, commonly Pauli spin blockade in double QDs [36] [Fig. 1(a)] or spin-selective tunneling to a reservoir through Zeeman splitting of the spin-up and -down energy levels in a single QD [37]. Recent experimental implementations of both SEBs [16] and SETs [24] have demonstrated strong capacitive coupling to the qubit, resulting in full modulation of the sensor from maximum admittance to Coulomb blockade in response to a single electronic charge. In this case, the qubit-readout problem reduces to detecting the presence or absence of a tunneling current in the sensor device, limited by intrinsic noise fluctuations in the tunneling current as well as technical noise sources due to amplification and demodulation. For weaker qubit-sensor interaction, changes in the magnitude and phase of the tunneling current, resulting in a correspondingly smaller change in the rf reflection coefficient, must be detected.

Considering in our analysis a single QD charging level, we model dot-to-reservoir tunneling in the thermally broadened regime ($\hbar\Gamma_0 < k_B T_e$ for a reservoir electron temperature T_e and a maximum tunnel rate Γ_0) as a Poissonian process with rate parameter [12]

$$\Gamma_{\text{in (out)}} = \frac{\Gamma_0}{1 + \exp\left\{\left(\mp\frac{V_g - V_0}{V_{\text{th}}}\right)\right\}}, \quad (1)$$

where V_0 is the voltage that aligns the dot level with the Fermi energy level of the reservoir and $V_{\text{th}} = k_B T_e/e\alpha$. Here, $\alpha = C_G/C_\Sigma$ is the gate lever arm with $C_\Sigma = (C_G + C_S)$, the sum of dot-gate capacitance C_G and tunnel barrier capacitance C_S. The stochastic evolution of the dot electron occupation number $Q(t)$ is described by the master equation [12]

$$\dot{P}_1(t, t_0) + \Gamma_0 P_1(t, t_0) = \Gamma_{\text{in}}(t), \quad (2)$$

where $P_1(t, t_0) \equiv \Pr\{(Q(t) = 1 | Q(t_0) = 1)\}$ for $t \geq t_0$, i.e., the probability of finding the QD occupied at time t given that it was occupied at time t_0. The solution for the initial condition $P_1(t_0, t_0) = 1$ can be written as

$$P_1(t, t_0) = P_{\text{SS}}(t) + e^{-\Gamma_0(t-t_0)}\left[1 - P_{\text{SS}}(t_0)\right], \quad (3)$$

where $P_{\text{SS}}(t)$ is the steady-state solution reached at times $t - t_0 \gg 1/\Gamma_0$:

$$P_{\text{SS}}(t) = e^{-\Gamma_0 t} \int e^{\Gamma_0 t} \Gamma_{\text{in}}(t)\, dt. \quad (4)$$

Under a small-signal gate excitation $V_g = V_{\text{dev}} \cos \omega_0 t$ with $V_{\text{dev}}/V_{\text{th}} \lesssim 1$ [Fig. 1(c)], Eq. (4) may be analytically evaluated by linearizing Eq. (1) as

$$\Gamma_{\text{in}}(V_g) \approx \frac{\Gamma_0}{1 + \exp(V_0/V_{\text{th}})} + \frac{\Gamma_0}{4\cosh^2(V_0/2V_{\text{th}})} \frac{V_g}{V_{\text{th}}}. \quad (5)$$

We arrive at an expression of the steady-state probability,

$$P_{\text{SS}}(t) = P_{\text{th}} + \frac{V_{\text{dev}}}{e\alpha\omega_0}\left(G_{\text{Sis}} \sin\omega_0 t + \omega_0 C_Q \cos\omega_0 t\right), \quad (6)$$

allowing the SEB to be represented by a small-signal admittance formed of a quantum capacitance and a Sisyphus conductance in parallel, $Y_Q(\omega_0) = \langle I_g(\omega_0)\rangle/V_{\text{dev}} = j\omega_0 C_Q + G_{\text{Sis}}$, through which a mean oscillatory gate current $\langle I_g\rangle = e\alpha\dot{P}_{\text{SS}}$ flows, as shown in the equivalent circuit in Fig. 1(b). Here,

$$P_{\text{th}} = \frac{1}{1 + \exp(V_0/V_{\text{th}})},$$
$$C_Q = \frac{e\alpha}{4V_{\text{th}}\cosh^2(V_0/2V_{\text{th}})} \frac{\Gamma_0^2}{\Gamma_0^2 + \omega_0^2}, \quad (7)$$
$$G_{\text{Sis}} = \frac{e\alpha}{4V_{\text{th}}\cosh^2(V_0/2V_{\text{th}})} \frac{\omega_0^2\Gamma_0}{\Gamma_0^2 + \omega_0^2}.$$

For a large gate excitation $V_g = V_{\text{dev}} \cos\omega_0 t$ with $V_{\text{dev}}/V_{\text{th}} \gg 1$, the SEB response becomes nonlinear as $\Gamma_{\text{in}}(t)$ in Eq. (1) approaches a square wave of amplitude Γ_0 and period $T = 2\pi/\omega_0$. A piecewise evaluation of Eq. (4) gives

$$P_{\text{SS}}(t) = \begin{cases} 1 - \beta e^{-\Gamma_0\left(t-\left(k-\frac{1}{4}\right)T\right)}, & k - \frac{1}{4} \leq \frac{t}{T} < k + \frac{1}{4}, \\ \beta e^{-\Gamma_0\left(t-\left(k+\frac{1}{4}\right)T\right)}, & k + \frac{1}{4} \leq \frac{t}{T} < k + \frac{3}{4}, \end{cases} \quad (8)$$

where $\beta = (1 + \exp(-\Gamma_0 T/2))^{-1}$ and k is an integer.

In order to calculate the noise current, we must consider the underlying random process, an ensemble of time traces $Q(t)$ of which $P_1(t, t_0)$ is the expectation value [Fig. 1(d)]. The master equation can be interpreted as the Kolmogorov forward equation for the time-inhomogeneous Markov

process

$$\Pr\{(Q(t + \delta t) = 1)\} = \begin{cases} \Gamma_{\text{in}}(t)\delta t, & Q(t) = 0, \\ 1 - \Gamma_{\text{out}}(t)\delta t, & Q(t) = 1. \end{cases} \quad (9)$$

Implementing this as an MMC simulation allows us to generate instances of the random process $Q(t)$ and verify the ensemble expectation $\langle Q(t) \rangle$ tends to $P_1(t)$ [Fig. 1(d)].

The noise spectrum is given by the Fourier transform of the autocorrelation function of the random process, $R_Q(t_0, t) = \mathbb{E}[Q(t_0)Q(t)]$, calculated from the joint probability that the dot is occupied at both times t_0 and t. For $t \geq t_0$, this can be understood in terms of conditional probabilities and expressed in terms of the solution to the master equation, as illustrated in Figs. 2(a) and 2(b):

$$R_Q(t_0, t) = \Pr(Q(t_0) = 1)\Pr(Q(t) = 1|Q(t_0) = 1)$$
$$= P_{\text{SS}}(t_0)P_1(t, t_0). \quad (10)$$

As both the ensemble mean, $P_{\text{SS}}(t)$, and the autocorrelation, $R_Q(t_0, t)$, are periodic $(R_Q(t_0, t) = R_Q(t_0 + kT, t + kT)$ for all integers $k)$, $Q(t)$ conforms to the definition of a cyclostationary process [32]. We can isolate the noise fluctuations by defining the random process $N(t) = Q(t) - \langle Q(t) \rangle$ with autocorrelation $R_N(t_0, t) = P_{\text{SS}}(t_0)(P_1(t_0, t) - P_{\text{SS}}(t))$ [Fig. 2(b)]. Under the transformation $\tau = t - t_0$, this can be expressed as a Fourier series of cyclic autocorrelation functions $R_N^{n\omega_0}(\tau)$,

$$R_N(t, \tau) = \sum_{n=-\infty}^{+\infty} R_N^{n\omega_0}(\tau)e^{jn\omega_0 t}, \quad (11)$$

plotted in Fig. 2(c) for $n = 0$ and 2, which are the orders that, as we derive below, contribute to the noise in rf reflectometry. The time scale over which the noise autocorrelation decays is set by the inverse of the tunnel rate Γ_0.

The Fourier transform of Eq. (11) gives the charge-noise spectrum $S_N(t, \omega)$ in terms of a series of spectral correlation functions, $S_N^{n\omega_0}(\omega)$. These are the equivalent of the noise harmonics in Ref. [33] and can be interpreted as the time-averaged correlation between frequency-shifted copies of the spectrum, $S_N^{\alpha}(\omega) = \overline{\langle S_N(t, \omega)S_N(t, \omega + \alpha) \rangle}^t$ [32]; the zeroth order is the time-averaged noise used to characterize the accuracy of single-electron emitters [30]. The transformation from dot charge fluctuations $eN(t)$ to gate-current noise is given by the Norton equivalent current $I_N = (e\alpha)dN/dt$ in parallel with C_S, which we treat as negligible in comparison to external parasitic capacitances. In terms of the spectral correlation functions, the transformation from charge to current noise is implemented
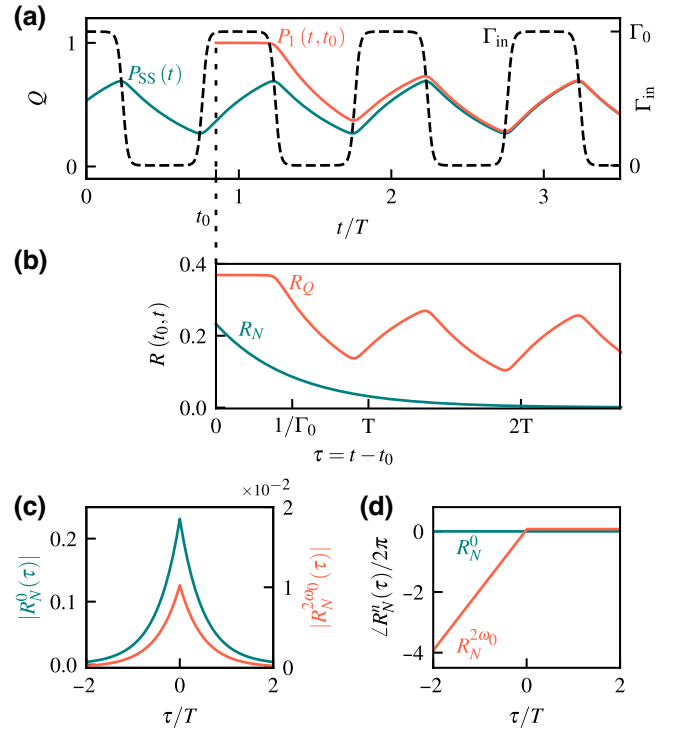

(a)

(b)

(c)

(d)

FIG. 2. The derivation of the cyclic autocorrelation functions. (a) The steady-state, $P_{\text{SS}}(t)$ (green), and conditional, $P_1(t, t_0)$ (orange), SEB occupation probabilities in response to a driving term $\Gamma_{\text{in}}(t)$ (dashed black) in the large-excitation regime $V_{\text{dev}}/V_{\text{th}} = 10$. The charge autocorrelation $R_Q(t, t_0)$ is given by their product, $P_{\text{SS}}(t)P_1(t, t_0)$ [(b), orange]; the noise autocorrelation R_N (green) is isolated by subtraction of the mean. (c) The magnitude and phase of the fundamental and second-harmonic cyclic autocorrelation functions (Fourier components of R_N), the orders that contribute to the measured noise in rf reflectometry.

as [32]

$$S_I^{n\omega_0}[\omega] = (e\alpha)^2 \omega(\omega - n\omega_0)S_N^{n\omega_0}[\omega]. \quad (12)$$

In the small-excitation limit, the $n = 0$ and 2 orders evaluate to (see Appendix A)

$$S_I^0(\omega) = \left[\frac{(e\alpha)^2}{2\cosh^2(V_0/2V_{\text{th}})} - \left(\frac{V_{\text{dev}}|Y_Q|}{\omega_0}\right)^2\right]\frac{\Gamma_0\omega^2}{\Gamma_0^2 + \omega^2}, \quad (13)$$

$$S_I^{2\omega_0} = -\left(\frac{V_{\text{dev}}Y_Q}{2\omega_0}\right)^2 \omega(\omega - 2\omega_0)$$
$$\times \left[\frac{1}{\Gamma_0 + j\omega} + \frac{1}{\Gamma_0 - j(\omega - 2\omega_0)}\right], \quad (14)$$

whereas for large excitation, the corresponding expressions are

$$S_I^0(\omega) = (e\alpha)^2 \frac{\omega_0}{\pi} \tanh\left(\frac{\pi\Gamma_0}{2\omega_0}\right) \frac{\omega^2}{\Gamma_0^2 + \omega^2}, \quad (15)$$

$$S_I^{2\omega_0}(\omega) = (e\alpha)^2 \frac{\omega_0}{\pi} \tanh\left(\frac{\pi\Gamma_0}{2\omega_0}\right) \omega(\omega - 2\omega_0)$$

$$\times \left[\frac{1}{\Gamma_0 + 2j\omega_0} - \frac{1}{2(\Gamma_0 + j\omega_0)}\right]$$

$$\times \left[\frac{1}{\Gamma_0 + j\omega} + \frac{1}{\Gamma_0 - j(\omega - 2\omega_0)}\right]. \quad (16)$$

It is worth noting that in the zero-excitation limit of Eq. (13), the noise spectral density at ω_0 tends to the Johnson-noise value predicted by the fluctuation-dissipation theorem using the Sisyphus conductance of the SEB: $S_I^0(\omega_0) = 2k_BT_eG_{Sis}$. Conversely, this does

not hold in the strongly driven case, where the out-of-equilibrium system dynamics do not obey detailed balance.

We now evaluate the spectral correlation functions and explain their physical meaning in different limits. In Fig. 3, we illustrate the dependence of the spectral correlation densities on the frequency, the tunnel rate, and the excitation amplitude, and compare the above analytical expressions to the numerical evaluation from the exact solution to the master equation $P_{SS}(t)$ propagated through Eqs. (10)–(12). In Fig. 3(a), we show the fundamental (S_I^0) and second-order ($S_I^{2\omega_0}$) spectral correlation functions in the small-excitation (solid lines) and large-excitation (dashed lines) regimes. The spectral densities tend to 0 at zero frequency, consistent with the zero dc current imposed by the cyclic tunneling, while tending to a flat (white-noise) spectrum in the high-frequency limit. Around the driving frequency ω_0, the portion of the
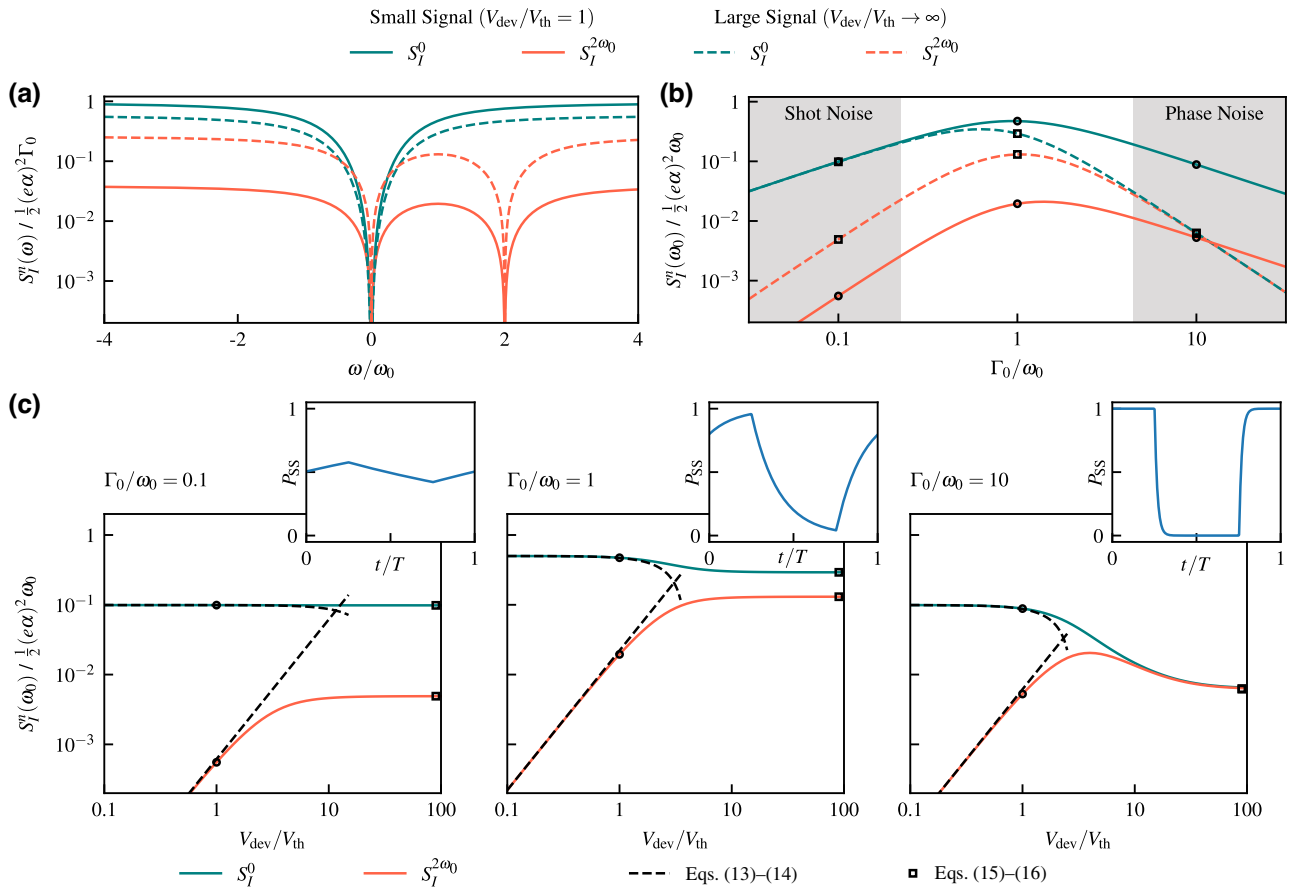

FIG. 3. The gate-current noise of the SEB quantified by the magnitude of the spectral correlation functions S_I^n, calculated from the numerical solution to the master equation $P_{SS}(t)$. (a) Fundamental (green) and second-order ($2\omega_0$ - orange) spectra for $\Gamma_0 = \omega_0$ in the small-excitation ($V_{dev}/V_{th} = 1$, solid lines) and large-excitation (dashed lines) regimes. (b) The dependence of the spectral density at ω_0 on the tunnel rate Γ_0 across the shot- and phase-noise ("quantum jitter") regimes (small to large Γ_0/ω_0) for small (solid) and large (dashed) excitations. (c)–(e) The system response in the shot-, intermediate-, and phase-noise regimes, including the dependence of the spectral density at ω_0 on excitation amplitude V_{dev} (green and orange, numerical calculations; dashed lines and square markers, analytical expressions) and the large-excitation steady-state dot charge response P_{SS} (inset). The circular (small excitation) and square (large excitation) markers indicated corresponding points in (b) and (c).

spectrum that we shall show contributes to the noise in rf reflectometry applications, there is a local maximum in the degree of correlation, as quantified by $S_I^{2\omega_0}$.

We can identify two contrasting regimes of operation for the intrinsic noise mechanism, the "shot-" and "phase-"noise regimes occurring in the limit of slow or fast tunnel rates compared to the excitation frequency, respectively [Fig. 3(b)]. In the limit of small Γ_0/ω_0—i.e., slow tunneling or fast excitation—tunneling occurs more rarely than each excitation period. The independent events result in shotlike noise with time-averaged spectral density $S_I^0(\omega)$ proportional to Γ_0, tending to the Schottky limit of $2e\langle I \rangle$ for a mean current $\langle I \rangle = e\Gamma_0/2$. Conversely, in the limit of large Γ_0/ω_0 (slow excitation), tunneling occurs each half-period of the drive, with noise arising from the exponentially distributed random times at which the tunneling event occurs within the period. This can be understood as phase noise or "quantum jitter" [29] and results in a time-averaged spectral density proportional to ω_0^2/Γ_0 (in the small-signal limit) or ω_0^3/Γ_0^2 (for large excitations), as can be seen from the slopes of the $n = 0$ orders at large Γ_0/ω_0 in Fig. 3(b). The noise is maximized in the intermediate regime (at $\Gamma_0/\omega_0 = 1$ for small excitations), which also corresponds to the conditions for maximum Sisyphus conductance [see Eq. (7)].

In Fig. 3(c), we study the dependence of the spectral correlation densities at ω_0 on the excitation amplitude $V_{\text{dev}}/V_{\text{th}}$ at three tunnel rates, $\Gamma_0/\omega_0 = 0.1$, 1, and 10, corresponding to the shot-, intermediate-, and phase-noise regimes, respectively. We find good agreement between the numerical and small-signal analytical expressions for $V_{\text{dev}}/V_{\text{th}} \lesssim 1$ and between the numerical and large-excitation expressions for $V_{\text{dev}}/V_{\text{th}} \gtrsim 50$. In each case, we observe two trends: the average noise power $S_I^0(\omega_0)$ decreases at large excitation amplitudes, while the "spectral coherence" [38], i.e., the ratio of spectral correlation densities $\rho = \left| S_I^{2\omega_0}(\omega_0)/S_I^0(\omega_0) \right|$, increases with the excitation amplitude. The decrease in $S_I^0(\omega_0)$ can be intuitively explained by considering $P_{\text{SS}}(t)$, which deviates further from 0.5 at large excitation amplitudes, corresponding to a reduced variance in $Q(t)$ and hence reduced noise current. As we shall discuss in Sec. III, the coherence plays an important role in noise enhancement or suppression during demodulation. We find that this is maximized in the phase-noise regime; again, the master-equation solutions $P_{\text{SS}}(t)$ in the high-$V_{\text{dev}}/V_{\text{th}}$ limit [see Fig. 3(c) insets] can help give an intuitive understanding. At large Γ_0/ω_0, $P_{\text{SS}}(t)$ approaches a square wave, indicating two near-deterministic tunneling events per cycle; these temporal correlations between cycles correspond to strong cyclostationary spectral correlations. By contrast, at small Γ_0/ω_0, the resultant $P_{\text{SS}}(t) \approx 0.5$ means that $Q(t)$ approaches a "random telegraph" signal, which does not exhibit any such correlations.

III. INTRINSIC SIGNAL-TO-NOISE RATIO

During spin-qubit readout with SEBs, a spin-dependent charge-tunneling event in the qubit shifts the SEB operation point by an amount ΔV_0 due to its capacitive coupling to the qubit (quantified here by the coupling lever arm, κ, given by the ratio of the mutual capacitance and total capacitance of the SEB),

$$\frac{\Delta V_0}{V_{\text{th}}} = \kappa \frac{e^2}{C_{\text{qubit}}} \frac{1}{k_B T_e}, \tag{17}$$

where C_{qubit} is the capacitance of the QD of the qubit. This produces a corresponding fractional change in the mean cyclic gate current of the SEB, $\eta = \langle \Delta I_g \rangle / \langle I_g^0 \rangle$, where $\langle I_g^0 \rangle$ is the mean gate current at $V_0 = 0$. In the small-signal limit, η can be expressed as $\eta = 1 - 1/\cosh^2(\Delta V_0/2V_{\text{th}})$. The readout task amounts to detecting this change in the presence of a gate-current noise spectral density S_I. Intuitively, the SNR over a measurement integration time τ_{int} would be given by $\left| \eta^2 \langle I_g^0(\omega_0) \rangle^2 \tau_{\text{int}}/S_I(\omega_0) \right|$; however, given the cyclostationary properties of S_I, the SNR can only be precisely defined in the context of synchronous demodulation (lock-in detection), as is used in rf reflectometry. In this section, we consider the idealized case of direct demodulation of the gate current I_g emitted by the SEB to determine the intrinsic SNR of the sensor without external factors such as the electrical resonator or amplifier noise; the effect of the resonator will be explored in Sec. V.

The signal-processing chain applied to the gate current $I_g(t)$, depicted in Fig. 4(a), consists of down-mixing by a local oscillator $\sqrt{2}\cos(\omega_c t + \varphi)$ with output $I_d(t)$ and image rejection through a low-pass filter $H_{\text{LP}}(\omega)$ to give a base-band signal $X(t,\varphi)$ that depends on the demodulation quadrature φ. Down-mixing produces a new cyclostationary signal $I_d(t)$ with cyclostationary orders $\nu \in \{n\omega_0 \cup n\omega_0 \pm 2\omega_c\}$, illustrated schematically in Fig. 4(b); we can write down the corresponding spectral density $S_D^\nu(\omega, \varphi)$ as [32]:

$$S_D^\nu(\omega, \varphi) = \frac{1}{2} \Big[S_I^\nu(\omega - \omega_c) + S_I^\nu(\omega + \omega_c) \\ + S_I^{\nu+2\omega_c}(\omega + \omega_c)e^{-j2\varphi} + S_I^{\nu-2\omega_c}(\omega - \omega_c)e^{j2\varphi} \Big]. \tag{18}$$

We are interested in the experimentally relevant case of homodyne detection with $\omega_c = \omega_0$, in which $I_d(t,\varphi)$ becomes a dc signal $X(\varphi)$ after the image-rejection filter H_{LP}. In this case, the cyclostationary orders of S_D^ν become $\nu \in n\omega_0$; given a filter cutoff frequency $\omega_{\text{LP}} < \omega_0/2$, the filter output X is then a wide-sense stationary process with spectral density $S_X(\omega, \varphi) = S_D^0(\omega, \varphi)$ for $|\omega| < \omega_{LP}$, since cyclostationary spectral correlations at frequencies separated by $\nu = n\omega_0$ cannot be supported by a signal

band limited to $|\omega| < \omega_0/2$ [32]. Evaluating Eq. (18) for $\omega_c = \omega_0$, we find that the low-frequency spectral density $S_X(\varphi) \equiv S_X(0, \varphi)$ after demodulation is given by

$$S_X(\varphi) = S_D^0(0, \varphi) = S_I^0(\omega_0) + \left| S_I^{2\omega_0}(\omega_0) \right| \cos(2\varphi + \theta),$$
(19)

where $\theta = \arg \left[S_I^{2\omega_0}(\omega_0) \right]$. Equation (19) demonstrates a key signature of the intrinsic noise of the SEB, one of the main results of our paper: cyclostationary spectral correlations—in particular, the orders $n = 0$ and ± 2 of $S_I^{n\omega_0}$—result in enhanced or suppressed noise depending on the local oscillator phase φ. For convenience, we notate this result as $S_X(\varphi) = S_X^0 + \Delta S_X \cos(2\varphi + \theta)$, where $S_X^0 = S_I^0(\omega_0)$ and $\Delta S_X = \left| S_I^{2\omega_0}(\omega_0) \right|$. Under conditions (as explored in Sec. II) in which the coherence $\rho = \left| S_I^{2\omega_0}(\omega_0)/S_I^0(\omega_0) \right| = \Delta S_X/S_X^0$ tends to 1, we can achieve near-complete suppression of the intrinsic noise in the demodulation quadrature $\varphi = (\pi - \theta)/2$.

In Figs. 4(c) and 4(d), we illustrate step by step the transformations described above, depicting both the signals and noise spectral densities at each stage from the device gate current and mixer output to the final low-pass-filtered baseband signal. The values are calculated for $\Gamma_0 = \omega_0$ in the large-excitation limit, conditions chosen to maximize both the signal I_g and the noise S_I^0 while also demonstrating the effect of a high degree of spectral coherence ($\rho = 0.45$). In the middle panel, two orthogonal local oscillator phases ($\varphi = \pi/4$ and $3\pi/4$) are shown, corresponding to standard in-phase and quadrature (I-Q) demodulation, with the quadrature axes chosen to align with the maximum and zero demodulator output signal, respectively. The phase dependence of the intrinsic noise of the SEB, a purely cyclostationary effect that contrasts with the phase independence of uncorrelated noise processes such as amplifier thermal noise, can clearly be seen in the differences between the spectra S_D^0 for the two quadratures [middle panel of Fig. 4(d)] and in the sinusoidal variation of $S_X(\varphi)$ [right-hand panel of Fig. 4(d)].

We can now accurately express the SNR of the qubit-readout measurement, accounting for the phase dependence of $X(\varphi)$ and $S_X(\varphi)$ and the difference in noise spectral density in either qubit state, as

$$\text{SNR} = \frac{\Delta X^2 \tau_{\text{int}}}{\left(\left| S_X^{|0\rangle} \right| + \left| S_X^{|1\rangle} \right| \right)/2},$$
(20)

where $\Delta X = X^{|0\rangle} - X^{|1\rangle} = \eta X^{|0\rangle}$ and $X^{|i\rangle}$ and $S_X^{|i\rangle}$ are the signal and noise corresponding to qubit state $|i\rangle$. In the limit of $\eta \to 1$, as is achieved in state-of-the-art experimental implementations with large qubit-sensor coupling [16,24,39], one qubit state corresponds to the sensor being in Coulomb blockade, i.e., both $X^{|1\rangle} = 0$ and $S_X^{|1\rangle} = 0$; in

this case, the SNR simplifies to $2(X^{|0\rangle})^2 \tau_{\text{int}}/S_X^{|0\rangle}$, plotted in Fig. 4(e). From Fig. 4(d), we see that the noise peaks and troughs do not necessarily correspond to the quadratures of maximum and zero signal; it follows that the optimum demodulator phase that maximizes the SNR is not the same as the phase that maximizes the signal [Fig. 4(e), solid line]. By contrast, omitting the effect of the cyclostationary spectral correlation $S_I^{2\omega_0}$ and accounting only for the time-averaged noise S_I^0 would predict an SNR that follows the phase dependence of the signal magnitude X^2, as shown by the dashed line in Fig. 4(e). In this example, exploiting the large cyclostationary spectral coherence boosts the SNR by 50% relative to the wide-sense stationary-noise case.

From the maximum phase-dependent SNR, we can benchmark the intrinsic sensitivity of the SEB, as characterized by the minimum integration time τ_{min} required to achieve an SNR = 1 [12]. Intuitively, in the case of a strong response ($\eta = 1$), states on and off Coulomb blockade could ideally be distinguished by a single tunneling event in the SEB, i.e., within a characteristic time $\tau_{\text{min}} \sim 1/\Gamma_0$; the analogous result for the SET would be the time taken for a single electron to transit the device, $\tau_{\text{min}} \sim e/\langle I \rangle$, where $\langle I \rangle$ is the average current flowing in the "ON" state [24]. For the parameters used in Fig. 4(e) ($\Gamma_0 = \omega_0$, in the large-excitation limit), we find a maximum of $X^2/S_X \approx \Gamma_0$ corresponding to $\tau_{\text{min}} \approx 1/2\Gamma_0$, consistent with the intuitive expectations. We must note, though, that the analysis of the homodyne demodulation scheme presented in this section is only applicable at readout bandwidths less than the cutoff frequency of the image-rejection filter, at most $\omega_0/2$ corresponding to $\tau_{\text{int}} > 2T$. Considering this experimental lower bound for the integration time, a measurement over two periods of the excitation signal would give an SNR $\approx 8\pi\Gamma_0/\omega_0$ and correspond to a readout fidelity of $F = 99.5\%$, as given by the standard expression

$$F = \frac{1}{2} \left[1 + \text{erf} \left(\sqrt{\frac{\text{SNR}}{8}} \right) \right].$$
(21)

We can perform an analogous calculation to determine the ultimate limits on the qubit-measurement bandwidth in the case of weaker qubit-sensor coupling, as occurs in architectures in which a single sensor is used for readout of multiple nearby qubits [5,16]. We consider a small shift $\Delta V_0 = V_{\text{th}}$ (resulting in $\eta = 0.2$ in the small-excitation limit) and choose an excitation amplitude of $V_{\text{dev}}/V_{\text{th}} = 1.7$ to maximize the signal ΔX; above this value, power broadening reduces the visibility of the states [40]. We now find a maximum of $\Delta X^2/S_X = 0.0035\Gamma_0$, corresponding to τ_{min} of 45 periods of the drive, while for a fidelity of 99.5%, an integration time τ_{int} of 1180 periods would be necessary. This large reduction in performance compared to the strong-response case can be attributed to a combination of five factors:
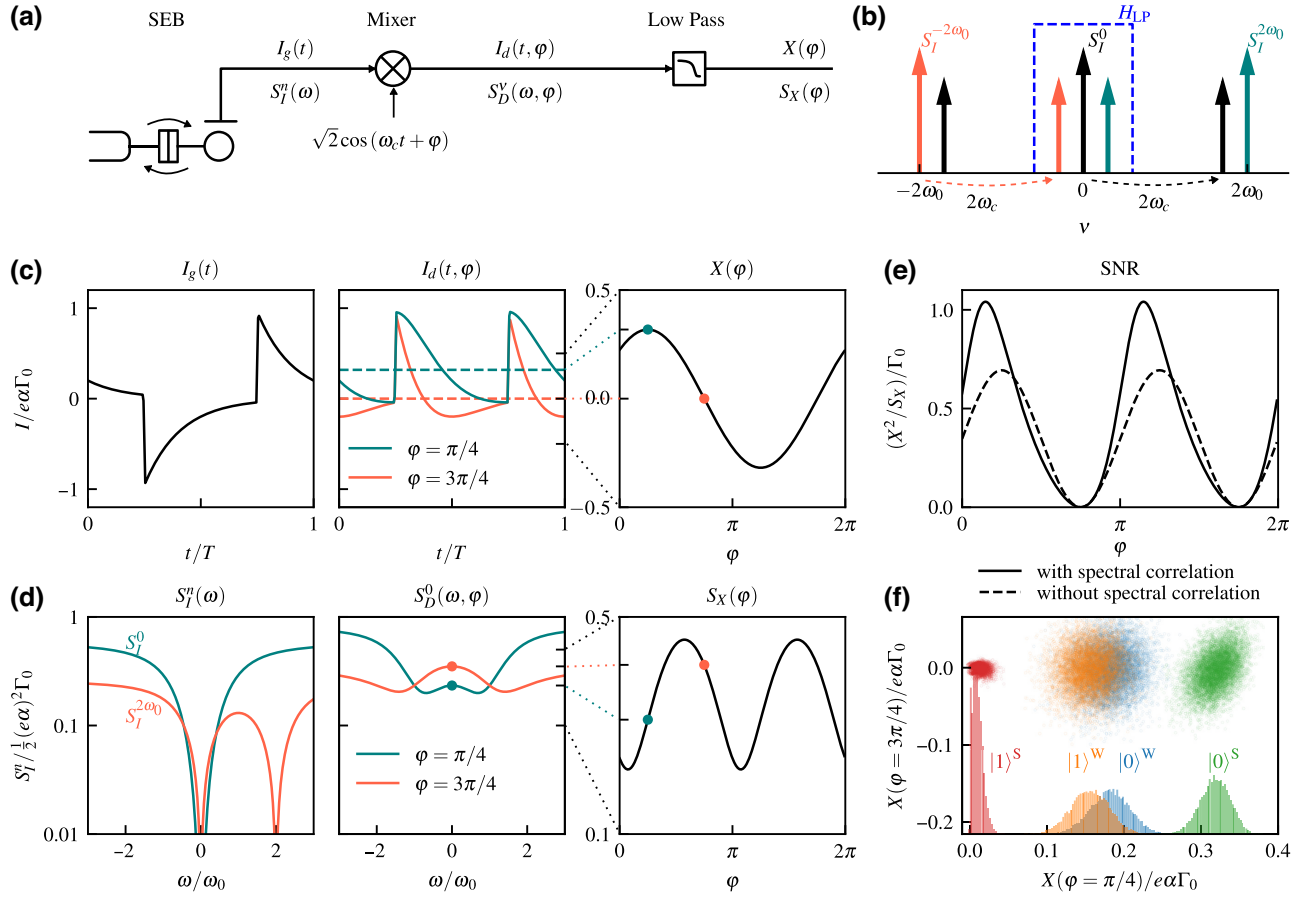
FIG. 4. The intrinsic signal-to-noise ratio (SNR) of the gate current of the SEB. (a) The synchronous demodulation scheme applied to the gate current I_g, consisting of down-mixing with a local oscillator of frequency ω_c and quadrature phase φ followed by low-pass filtering with transfer function H_{LP}. The signals I_g, I_d, and X at each stage of demodulation and the corresponding noise spectra S_I, S_D, and S_X are illustrated in (c) and (d), respectively. (b) The generation of the cyclostationary orders ν of the mixer output (I_d) from the input spectral correlation functions $S_I^{n\omega_0}$ and the local-oscillator-frequency ω_c ($S_I^{\pm\omega_0}$ orders are omitted for clarity); the pass band of the image-rejection filter with transfer function H_{LP} is shown in blue. (c) Example signal wave forms and (d) noise spectra in the large-excitation limit with $\omega_0 = \Gamma_0$ and $\omega_c = \omega_0$. In the middle panel, two demodulation quadratures $\varphi = \pi/4$ and $3\pi/4$ corresponding to the minimum and maximum demodulated signal are shown. The output of the low-pass filter X is the dc component of the down-mixed wave form I_d (dashed lines). (e) The resultant SNR as a function of the demodulation quadrature φ, both with and without the effect of the cyclostationary spectral correlation $S_I^{2\omega_0}$. (f) MMC simulations of the qubit-readout fidelity in the strong (S) and weak (W) response regimes with an integration time $\tau_{\text{int}} = 50T$. Histogram and I-Q data points of 10^4 shots for the demodulation quadratures $\varphi = \pi/4$ and $3\pi/4$.

(i) a reduction in the fractional change in signal by $1/\eta^2$ (a factor of approximately 50, as the exact value of η reduces to 0.14 due to the nonlinear response for $V_{\text{dev}} > V_{\text{th}}$),

(ii) a reduction in the absolute gate current $\langle I_g^0 \rangle$ due to the power-broadening limits on excitation amplitude (a factor of 3),

(iii) the presence of intrinsic noise in the SEB now in both qubit states (a factor of 2),

(iv) an increase in the average noise S_I^0 at small excitation amplitudes (a factor of 1.4 - cf. Fig. 3(c), middle panel), and

(v) a decrease in the spectral coherence and the noise suppression it offers at the optimum phase.

We can verify and illustrate these results for the ultimate fidelity of the SEB using MMC simulations. In Fig. 4(e), we plot on the complex (I-Q) plane the demodulated signal of 10^4 shots for each qubit state with an integration time $\tau_{\text{int}} = 50T$; we choose the demodulation quadratures to correspond to the maximum and zero signal ($\varphi = \pi/4$ and $3\pi/4$, respectively). In particular, we plot data clouds for the qubit states $|0\rangle$ and $|1\rangle$ in the strong-response regime (green and red, respectively) and in the weak regime (blue and orange). In the strong-response regime (using simulation parameters $\Gamma_0 = \omega_0$, $\Delta V_0 = 25V_{\text{th}}$, and $V_{\text{dev}} = 23V_{\text{th}}$), the histograms of the demodulated signal for either state in the $\varphi = \pi/4$ quadrature exhibit no overlap, indicating a fidelity exceeding 99.99%. We see that

the "OFF" state of the SEB (corresponding to the qubit $|1\rangle$ state, red) has much reduced noise compared to the "ON" state ($|0\rangle$, green); further, the effect of spectral correlation in the "ON" state at large excitation amplitudes is evident in the anisotropic distribution of points in the I-Q plane. In the weak-response case ($\Delta V_0 = V_{th}$, $V_{dev} = 1.7 V_{th}$), there is a large degree of overlap in the distribution of points for either qubit state; the intrinsic noise of the SEB is significant in both qubit states and the reduced spectral coherence (due to the reduced excitation amplitude) results in near-circular distributions. The resultant fidelity is reduced to 70.4%, corresponding to an SNR of 1.07, in line with the analytical calculation of $\tau_{min} = 45T$.

IV. SEB-INDUCED BACK ACTION

Coupling the SEB to a qubit can lead to dephasing and relaxation, with this back action mediated by fluctuations of the voltage V_{QD} on the SEB QD both during and in between measurement operations. The stochastic dot charge $Q(t)$ and the periodic gate drive $V_g(t)$ both contribute to the fluctuations $V_{QD}(t) = -eQ(t)/C_\Sigma + \alpha V_g(t)$, which result in a noise term $S_V(\omega)$ arising from the charge-noise autocorrelation R_N, as well as a harmonic driving term due to the periodic $V_g(t)$ and $P_{SS}(t)$ (see Appendix B):

$$S_V(\omega) = \left(\frac{e}{C_\Sigma}\right)^2 S_N^0(\omega) = \left(\frac{1}{\omega C_G}\right)^2 S_I^0(\omega). \qquad (22)$$

The back-action-induced relaxation rate Γ_1 of a qubit $|0\rangle$, $|1\rangle$ with Hamiltonian H_Q is proportional to the noise spectral density at the qubit frequency ω_q and is given by the well-known formula [12,23]:

$$\Gamma_1 = \frac{1}{T_1} = \frac{1}{2\hbar^2} \left| \langle 0| \frac{\partial H_Q}{\partial V_{QD}} |1\rangle \right|^2 S_V(\omega_q). \qquad (23)$$

The harmonic component of V_{QD} can be separately considered as driving Rabi oscillations (negligible if $\omega_q \neq n\omega_0$). On the other hand, the dephasing rate Γ_ϕ can be expressed in terms of the low-frequency noise [12],

$$\Gamma_\phi = \frac{1}{T_2^*} = \frac{1}{4} \left(\frac{\partial \omega_q}{\partial V_{QD}}\right)^2 S_V(0), \qquad (24)$$

while a constant shift in the qubit frequency due to the dc term of V_{QD}, eP_{th}/C_Σ, may be accounted for separately.

We consider the example of a double-QD (DQD) charge qubit with interdot tunnel coupling Δ_c, operated at interdot energy detuning ε_0 and capacitively coupled with lever arm κ to the SEB. Given the Hamiltonian of the system $H_{DQD} = \frac{1}{2}(\varepsilon\sigma_z + \Delta_c\sigma_x)$ and the total detuning $\varepsilon = \varepsilon_0 + \kappa V_{QD}$, we find the following SEB-induced relaxation

and dephasing rates:

$$\Gamma_1 = \frac{1}{2\hbar^2} \left(\frac{e\kappa\Delta_c}{2\hbar\omega_q}\right)^2 \left(\frac{e}{C_\Sigma}\right)^2 S_N^0(\omega_q), \qquad (25)$$

$$\Gamma_\phi = \frac{1}{4\hbar^2} \left(\frac{e\kappa\varepsilon_0}{\hbar\omega_q}\right)^2 \left(\frac{e}{C_\Sigma}\right)^2 S_N^0(0). \qquad (26)$$

V. APPLICATION TO RF REFLECTOMETRY

Having fully characterized the cyclostationary-noise spectrum and the intrinsic SNR of the gate current of the SEB, we turn our attention to the application of SEB readout via rf reflectometry, now including the effect of the resonator. The resonator primarily acts as a band-pass filter on the current noise spectrum emitted into the transmission line; however, we shall see that excitation of the resonator by the intrinsic noise of the SEB can itself incoherently drive electron tunneling. This back action leads to deviations from a pure cyclostationary process, becoming significant at low reflectometry powers (small V_f), where the noise excitation on the gate voltage dominates over the coherent sinusoidal drive.

The signal-processing chain corresponding to the reflectometry circuit in Fig. 1(b) is depicted in Fig. 5(a) and consists of band-pass filtering through the resonator with transfer function $H_{IB}(\omega)$ from gate current I_g to transmission-line wave $V_b(t)$, followed by synchronous demodulation of $V_b(t)$ as described in Sec. III (down-mixing and low-pass filtering). In terms of the spectral correlation functions, filtering by the resonator is represented by [32]

$$S_B^{n\omega_0}(\omega) = S_I^{n\omega_0}(\omega)H_{IB}(\omega)H_{IB}^*(\omega - n\omega_0), \qquad (27)$$

where, for a capacitively coupled parallel *LCR* resonator,

$$H_{IB}(\omega) = \frac{j\omega C_c Z_0}{(Y_Q + Y_{res})(1 + j\omega C_c Z_0) + j\omega C_c}, \qquad (28)$$

using $Y_{res} = j\omega C_r + 1/(j\omega L_r) + G_r$ with the lumped-element resonator values (capacitance C_r, inductance L_r, loss conductance G_r, and coupling capacitance C_c) and transmission-line impedance Z_0 shown in Fig. 1(b). This allows a self-consistent solution that includes the effect of the small-signal admittance Y_Q of the SEB loading the resonator. Note that in the large-signal limit, power broadening of the quantum capacitance and Sisyphus resistance means that Y_Q tends to zero [40]; for intermediate powers, the reduction of Y_Q can be directly calculated from the fundamental (ω_0) Fourier component of $P_{SS}(t)$ or, equivalently, by using a describing function approach [16,40,41].

In Figs. 5(b)–5(e), we illustrate the noise spectra $S_I^{n\omega_0}$, $S_B^{n\omega_0}$, S_D^0, and S_X corresponding to the signals at each
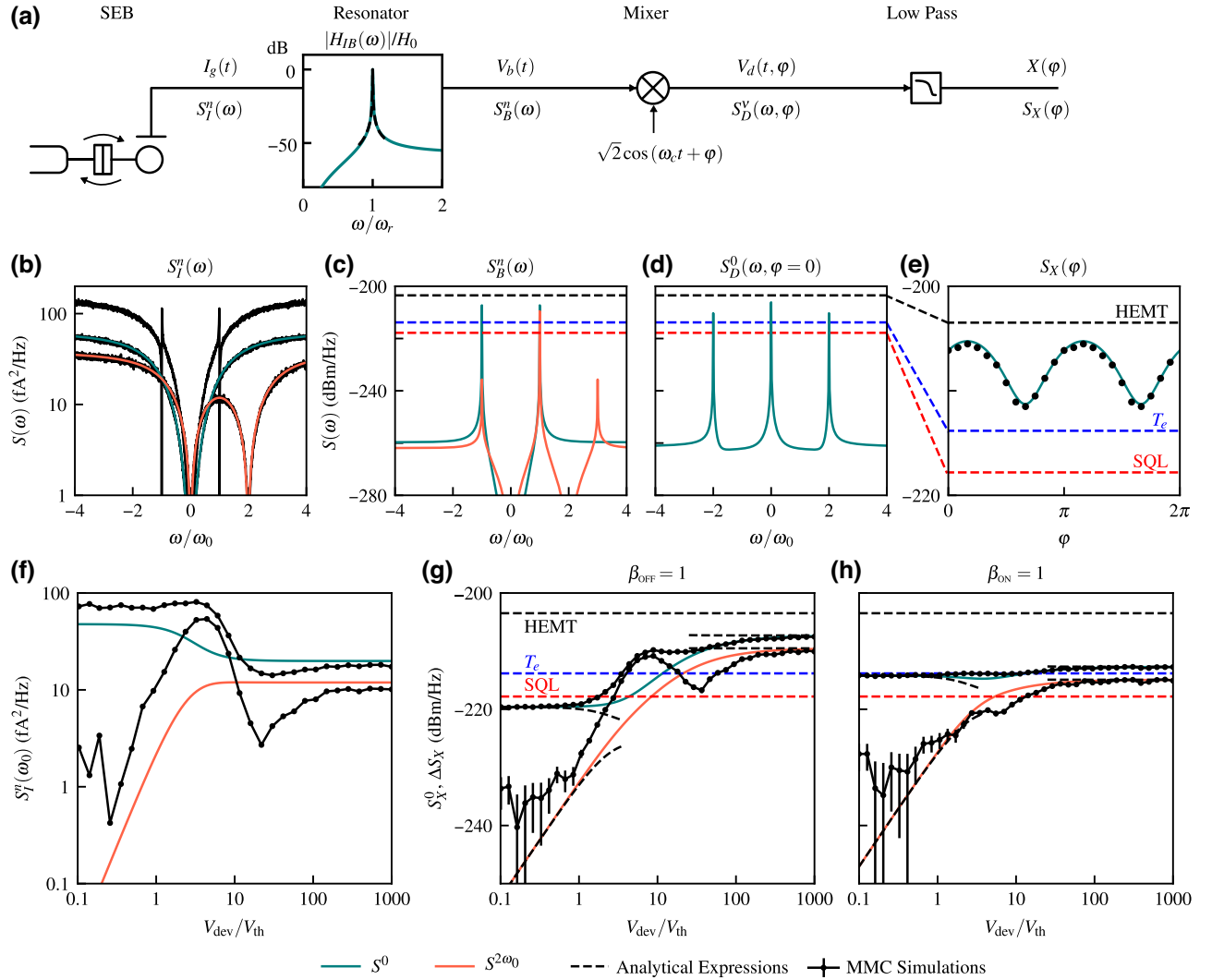
FIG. 5.   The intrinsic noise of the SEB in rf reflectometry and the efficiency of transmission through the resonator. (a) The signal-processing chain associated with the reflectometry circuit in Fig. 1(b). The exact [Eq. (28), solid line] and approximated [Eq. (29), dashed line] resonator transfer functions H_{IB} are plotted in the inset, normalized to the peak value H_0. (b)–(e) Noise spectra corresponding to each signal in the chain, calculated for typical experimental parameter values (with $\beta_{OFF} = 1$) in the large-excitation limit. The black markers are the corresponding MMC simulation results; (b) includes spectra in the small- (upper line) and large- (lower line) excitation limits. The dashed lines correspond to the noise power associated with cryogenic HEMT amplifiers (black), the electron temperature T_e (blue) and the standard quantum limit (SQL, red). (f) The dependence of the noise current on the excitation amplitude and (g),(h) the corresponding demodulated noise power transmitted through two different resonator designs, critically coupled in the unloaded (g) and loaded (h) states, respectively. Analytical (dashed), numerical (solid), and MMC simulation (black marker) results are plotted, with HEMT, electron temperature, and SQL noise powers included for comparison. The MMC data in (f) correspond to the parameters in (g) and are independently calculated from the MMC time trace $Q(t)$.

stage in the reflectometry chain: the gate current I_g, the reflected wave V_b, the down-mixed signal V_d, and the low-pass-filtered output X. These are calculated in the large-excitation limit and for resonator parameters similar to those seen in recent experimental implementations [42]: resonator frequency $\omega_r = \omega_0 = \omega_c = 2\pi \times 2\,\text{GHz}$, internal quality factor $Q_i = 2000$, coupling coefficient $\beta = 1$, transmission-line impedance $Z_0 = 50\,\Omega$ and SEB parameters $\Gamma_0/\omega_0 = 1.5$, $T_e = 120\,\text{mK}$, and $\alpha = 0.8$ [41].

We include for comparison the spectral densities corresponding to the noise temperatures of state-of-the-art cryogenic HEMT amplifiers (1.3 K [12,43], black dashed line) and the electron temperature T_e (120 mK, blue dashed line), as well as the standard quantum limit (SQL) of $\hbar\omega_0/2$ (red dashed line) approached by current parametric amplifier implementations [44,45]. The demodulated noise spectral density S_X [Fig. 5(e)] shows the expected sinusoidal dependence on demodulator phase, which we verify

with MMC simulations (black markers; discussed further below and in Appendix C). The spectral density can clearly exceed the standard quantum limit and approach that of the HEMT; this suggests the intrinsic noise of the SEB may directly limit the fidelity of gate-based readout methods in certain resonator and device-parameter regimes that we explore next.

In particular, we shall consider how the effective noise power in rf reflectometry depends not only on the noise current S_I of the SEB but also on the efficiency with which the noise current is coupled into the transmission line. This is a function of the resonator design; specifically, the quality factor Q_i and coupling coefficient β, as well as the degree of loading of the resonator by the admittance Y_Q of the SEB. This can be readily seen by considering the approximated form of Eq. (28),

$$H_{IB}(\omega) \approx \frac{\sqrt{KZ_0}}{K + G_r + 2j(\omega - \omega_r)C_t + Y_Q},\qquad(29)$$

where we define $K = \beta G_r = \omega_r^2 C_c^2 Z_0$ and $C_t = C_r + C_c$. For the bare resonator, i.e., with the SEB in Coulomb blockade ("OFF") or strongly overdriven such that Y_Q tends to zero, the maximum $|H_{IB}|^2/Z_0 = 1/4G_r$ is achieved on resonance ($\omega = \omega_r$) with critical coupling of the bare resonator ($K = G_r$, i.e., $\beta_{\text{OFF}} = 1$). With the SEB in the unblockaded "ON" state, loading due to Y_Q reduces the maximum to $|H_{IB}|^2/Z_0 = 1/4(G_r + G_{\text{Sis}})$, achieved on the dispersively shifted resonance ($\omega = \omega_r/(1 + C_Q/2C_t)$) and with critical coupling of the loaded resonator ($K = G_r + G_{\text{Sis}}$, i.e., $\beta_{\text{ON}} = 1$). We see, therefore, that the resonator parameters act in conjunction with the effective admittance of the SEB to determine the frequency and excitation amplitude at which the noise is most efficiently coupled.

We demonstrate the above results in Figs. 5(f)–5(h) by calculating, as a function of the excitation amplitude, the noise transmitted through two different resonator designs: in Fig. 5(g), for a resonator critically coupled in the unloaded state ($\beta_{\text{OFF}} = 1$) and, in Fig. 5(h), for a resonator critically coupled in the loaded state ($\beta_{\text{ON}} = 1$, using a larger value of C_c). Though the gate-current noise of the SEB is, according to our analytical framework, the same for both resonator designs [Fig. 5(f), cf. Fig. 3(c)], the noise-coupling efficiency into the transmission line, and the excitation amplitude at which this is maximized, differ. For the first resonator ($\beta_{\text{OFF}} = 1$), the coupling efficiency is maximized in the strongly overdriven limit when operating at $\omega_0 = \omega_r$, giving a peak value of the average noise of $S_X^{\max}/Z_0 = S_I^0(\omega_0)/4G_r$, indicated by the horizontal black dashed lines at high V_{dev} in Fig. 5(g). Conversely, for the second design ($\beta_{\text{ON}} = 1$), the noise is coupled efficiently in the small-signal regime—although in our example, Sisyphus losses reduce the effective Q_i and hence the efficiency compared to the overdriven regime. In the small-excitation

limit with a high-Q resonator ($G_{\text{Sis}} \gg G_r$), the intrinsic noise power of the SEB at the dispersively shifted frequency corresponds to Johnson noise at the reservoir electron temperature: $S_X^{\max}/Z_0 = k_B T_e/2$ [Fig. 5(h)]. We interpolate between the analytical results in the small-signal and large-signal regimes using numerical calculations of both $S_I^{n\omega_0}$ and Y_Q as described above, while tracking the dispersive shift in resonance frequency due to the quantum capacitance with ω_0 [green and orange solid lines in Figs. 5(g) and 5(h)]. However, as we discuss next, our autocorrelation-based model cannot fully capture the dynamics of the hybrid system: the effective admittance Y_Q in the nonlinear regime is only valid at the excitation frequency and cannot represent the response to wide-band noise, while our analysis assumes the gate voltage V_g to be a noiseless sinusoid.

To improve upon our above calculations and investigate the effect of noise-driven tunneling, we resort to MMC simulations of the complete circuit, including the SEB, the resonator, and synchronous demodulation. The ring-down time of the resonator induces memory into the combined system, as captured by its step response to each electron-tunneling event. Augmenting the model in Eq. (9) with the non-Markovian dynamics of the resonator can then be represented by the convolution

$$V_{g(b)}(t) = \text{Re}\left(H_{FG(FB)}(\omega_0)V_f e^{j\omega_0 t}\right)$$
$$+ \int_{-\infty}^{t} I_g(\tau)h_{IG(IB)}(t-\tau)\,d\tau,\qquad(30)$$

where $H_{FG(FB)}(\omega)$ is the resonator transmission (reflection) coefficient $V_{g(b)}/V_f$ and $h_{IG(IB)}(t)$ is the gate-current impulse response (i.e., charge step response) of $V_{g(b)}(t)$; we implement the convolution using an infinite impulse-response digital filter (see the details in Appendix C). S_X^0 and ΔS_X [black markers in Figs. 5(g) and 5(h)] are extracted from the phase-dependent $S_X(\varphi)$ [cf. Fig. 5(e)], with the mean and standard error calculated from 500 trials of duration 2^{14} cycles with a step size $\Delta t = T/2^{11}$.

The simulations show good agreement with the master-equation analysis when the resonator is strongly coupled to the transmission line [a large C_c as in Fig. 5(h)] or in the limit of large excitation powers. However, for weaker resonator–transmission-line coupling, as is seen in Fig. 5(g), significant discrepancies occur at low and intermediate excitation powers; in this example, we observe increases in both the average noise and the degree of cyclo-stationary correlation around $V_{\text{dev}}/V_{\text{th}} = 10$. This suggests that the non-Markovian dynamics and incoherent excitation of the resonator by the SEB, which are not captured in our autocorrelation analysis, can no longer be neglected when the resonator response to individual tunneling events is large compared to the periodic drive. The discrepancy can be traced back to the current noise emitted by the SEB

[black markers in Fig. 5(f)], which we compute directly from the MMC time series $Q(t)$ (see Appendix C). The corresponding spectrum for the zero-excitation limit [upper black line in Fig. 5(b)] demonstrates a sharp perturbation around the frequency of the resonator but conforms to the analytical results in the large-excitation limit [lower black line in Fig. 5(b)]. The noise peak seen at intermediate powers in Figs. 5(f) and 5(g) can be explained by the operating frequency ω_0 sweeping across this perturbation around ω_r as we track the dispersive shift. However, for a deeper understanding of the interactions occurring in the hybrid SEB-resonator system, a full analysis of the underlying stochastic differential equations would be necessary.

VI. CONCLUSIONS

We have addressed the lack of a noise model applicable to rf readout of the single-electron box, an increasingly widespread technology in the development of semiconductor quantum computing architectures. Starting from a semiclassical model of stochastic electron tunneling between a QD and a reservoir driven by a periodic gate excitation, we have described the noise mechanism as a cyclostationary processes to derive and develop analytical expressions, numerical models, and MMC simulations for the gate-current noise. Our analytical framework is able to precisely capture the correlations that arise in the noise spectrum and the interference that results upon demodulation or lock-in detection of the SEB signal, which manifests as phase-dependent noise enhancement or suppression.

In addition to characterizing the gate-noise current of the SEB, we have studied its practical application to qubit readout by rf reflectometry, considering the dynamics of the combined SEB-resonator system and evaluating the noise power under typical experimental parameters. The resonator design determines the efficiency by which the noise current of the SEB is emitted into the transmission line; with the resonator critically coupled to the line ($\beta = 1$), we find that the emitted noise power can approach that of cryogenic HEMT amplifiers. Conversely, under weak resonator-line coupling and small rf drive powers, excitation of the resonator by the intrinsic noise of the SEB can itself incoherently drive electron tunneling. Rich interaction dynamics within the hybrid SEB-resonator system emerge, which we can probe with MMC simulations but that are beyond the capacity of our autocorrelation-based analytical approach.

With the introduction of parametric amplifier-enhanced QD readout hardware, we expect signatures of the intrinsic noise of the SEB to be measured in the near future. This will allow the experimental realization of schemes to achieve a high degree of noise suppression by exploiting spectral correlations, thereby enhancing the fidelity of spin-qubit readout with SEBs.

APPENDIX A: DERIVATION OF THE CYCLOSTATIONARY SPECTRAL CORRELATION FUNCTIONS

Under the transformation $\tau = t - t_0$, the noise autocorrelation can be expressed as

$$R_N(t, \tau) = R_Q(t, \tau) - P_{SS}(t)P_{SS}(t + \tau), \quad \text{(A1)}$$

with

$$R_Q(t, \tau) = h(\tau)P_{SS}(t)P_1(t + \tau, t) \\ + h(-\tau)P_{SS}(t + \tau)P_1(t, t + \tau), \quad \text{(A2)}$$

where $h(\tau)$ is the Heaviside step function. Inserting Eq. (6), the solution to the linearized master equation, into Eq. (A1),

$$R(t, \tau) = h(\tau)e^{-\Gamma_0\tau}P_{SS}(t)(1 - P_{SS}(t)) \\ + h(-\tau)e^{\Gamma_0\tau}P_{SS}(t + \tau)(1 - P_{SS}(t + \tau)), \quad \text{(A3)}$$

and equating terms with Eq. (11), we find that the Fourier decomposition of $R_N(t, \tau)$ can be written as

$$R_N^0(\tau) = \left[\frac{1}{4\cosh^2(V_0/2V_{th})} - \frac{1}{2}\left(\frac{V_{dev}|Y_Q|}{e\alpha\omega_0}\right)^2\right]e^{-\Gamma_0|\tau|}, \quad \text{(A4)}$$

$$R_N^{\omega_0}(\tau) = \frac{V_{dev}Y_Q}{e\alpha\omega_0}\left(\frac{1}{2} - P_{th}\right) \\ \times \left[h(\tau)e^{-\Gamma_0\tau} + h(-\tau)e^{\Gamma_0\tau}e^{j\omega\tau}\right], \quad \text{(A5)}$$

$$R_N^{2\omega_0}(\tau) = -\left(\frac{V_{dev}Y_Q}{2e\alpha\omega_0}\right)^2\left[h(\tau)e^{-\Gamma_0\tau} + h(-\tau)e^{\Gamma_0\tau}e^{2j\omega\tau}\right], \quad \text{(A6)}$$

with $R_N^{-\omega_0}(\tau)$ and $R_N^{-2\omega_0}(\tau)$ given by the complex conjugates of $R_N^{\omega_0}(\tau)$ and $R_N^{2\omega_0}(\tau)$. Taking the Fourier transform of the above cyclic autocorrelation functions gives the set of charge-noise spectral correlation functions:

$$S_N^0(\omega) = \left[\frac{1}{4\cosh^2(V_0/2V_{\text{th}})} - \frac{1}{2}\left(\frac{V_{\text{dev}}|Y_Q|}{e\alpha\omega_0}\right)^2 \right] \frac{2\Gamma_0}{\Gamma_0^2 + \omega^2}, \tag{A7}$$

$$S_N^{\omega_0}(\omega) = \frac{V_{\text{dev}}Y_Q}{e\alpha\omega_0}\left(\frac{1}{2} - P_{\text{th}}\right)\left[\frac{1}{\Gamma_0 + j\omega} + \frac{1}{\Gamma_0 - j(\omega - \omega_0)}\right], \tag{A8}$$

$$S_N^{2\omega_0} = -\left(\frac{V_{\text{dev}}Y_Q}{2e\alpha\omega_0}\right)^2\left[\frac{1}{\Gamma_0 + j\omega} + \frac{1}{\Gamma_0 - j(\omega - 2\omega_0)}\right]. \tag{A9}$$

Similarly, inserting Eq. (8) into Eq. (A3) and considering the Fourier series of the resulting wave form,

$$P_{\text{SS}}(t)\,(1 - P_{\text{SS}}(t)) = \beta e^{-\Gamma_0(t+T/4)}\left(1 - \beta e^{-\Gamma_0(t+T/4)}\right) \tag{A10}$$

for $-T/4 \le t < T/4$, we derive the results for the large-excitation limit:

$$R_N^0(\tau) = \frac{\omega_0}{2\pi\Gamma_0}\tanh\left(\frac{\pi\Gamma_0}{2\omega_0}\right)e^{-\Gamma_0|\tau|}, \tag{A11}$$

$$R_N^{2\omega_0}(\tau) = \frac{\omega_0}{\pi}\tanh\left(\frac{\pi\Gamma_0}{2\omega_0}\right)\left[\frac{1}{\Gamma_0 + 2j\omega_0} - \frac{1}{2(\Gamma_0 + j\omega_0)}\right]\left[h(\tau)e^{-\Gamma_0\tau} + h(-\tau)e^{\Gamma_0\tau}e^{2j\omega\tau}\right], \tag{A12}$$

$$S_N^0(\omega) = \frac{\omega_0}{\pi}\tanh\left(\frac{\pi\Gamma_0}{2\omega_0}\right)\frac{1}{\Gamma_0^2 + \omega^2}, \tag{A13}$$

$$S_N^{2\omega_0}(\omega) = \frac{\omega_0}{\pi}\tanh\left(\frac{\pi\Gamma_0}{2\omega_0}\right)\left[\frac{1}{\Gamma_0 + 2j\omega_0} - \frac{1}{2(\Gamma_0 + j\omega_0)}\right]\left[\frac{1}{\Gamma_0 + j\omega} + \frac{1}{\Gamma_0 - j(\omega - 2\omega_0)}\right]. \tag{A14}$$

Note that due to the symmetry of $P_{\text{SS}}(t)$, the first-order terms $R_N^{\omega_0}(\tau)$ and $S_N^{\omega_0}(\omega)$ are zero.

APPENDIX B: BACK ACTION

We are interested in the time-averaged autocorrelation of the voltage fluctuations $V_{\text{QD}}(t)$ on the QD of the SEB, $R_V^0(\tau)$, which can be calculated from

$$R_V(t_1, t_2) = \mathbb{E}\left[V_{\text{QD}}(t_1)V_{\text{QD}}(t_2)\right] = \frac{e^2}{C_\Sigma^2}\mathbb{E}\left[Q(t_1)Q(t_2)\right] + \alpha^2 V_g(t_1)V_g(t_2) - \frac{e\alpha}{C_\Sigma}\left[\mathbb{E}\left[Q(t_1)\right]V_g(t_2) + \mathbb{E}\left[Q(t_2)\right]V_g(t_1)\right]. \tag{B1}$$

Recognizing that $\mathbb{E}\left[Q(t_1)Q(t_2)\right] = R_Q(t_1, t_2)$ and $\mathbb{E}\left[Q(t)\right] = P_{\text{SS}}(t)$, we can write down

$$R_V(t_1, t_2) = \frac{e^2}{C_\Sigma^2}R_N(t_1, t_2) + \frac{e^2}{C_\Sigma^2}P_{\text{SS}}(t_1)P_{\text{SS}}(t_2) - \frac{e\alpha}{C_\Sigma}\left[P_{\text{SS}}(t_1)V_g(t_2) + P_{\text{SS}}(t_2)V_g(t_1)\right] + \alpha^2 V_g(t_1)V_g(t_2). \tag{B2}$$

The first term gives the time-averaged voltage noise associated with charge fluctuations $S_V(\omega)$ (from the Fourier transform of $R_V^0(\tau) = (e^2/C_\Sigma^2)R_N^0(\tau)$). Evaluating the complete expression in the small-signal limit gives

$$R_V^0(\tau) = \frac{e^2}{C_\Sigma^2}R_N^0(\tau) + \frac{e^2}{C_\Sigma^2}P_{\text{th}}^2 + \frac{\cos\omega_0\tau}{2}\left[\alpha^2 V_{\text{dev}}^2 + \frac{e^2}{C_\Sigma^2}\left(\frac{V_{\text{dev}}|Y_Q|}{e\alpha\omega_0}\right)^2 + \frac{2e\alpha}{C_\Sigma}\left(\frac{V_{\text{dev}}^2 G_{\text{Sis}}}{e\alpha\omega_0}\right)\right], \tag{B3}$$

where the remaining terms can be identified as due to the harmonic component of the QD voltage,

$$V_{\text{QD}}^H(t) = \frac{eP_{\text{th}}}{C_\Sigma} + \text{Re}\left\{\left(\frac{Y_Q}{\alpha j\omega_0 C_\Sigma} + \alpha\right)V_{\text{dev}}e^{j\omega_0 t}\right\}. \tag{B4}$$

Note that additional terms at frequencies $n\omega_0$ would arise in $V_{\mathrm{QD}}^H(t)$ in the large-excitation due to harmonic distortion in the exact solution to the nonlinear master equation.

APPENDIX C: MARKOV MONTE CARLO SIMULATIONS

We discretize the time-inhomogeneous Markov process introduced in Eq. (9) at N_Δ samples per cycle period $T = 2\pi/\omega_0$, with successive samples $Q_k = Q(kT/N_\Delta)$ calculated from

$$Q_{k+1} = R_k^+ + (1 - R_k^+ - R_k^-)Q_k, \qquad (\text{C1})$$

where the tunneling in (out) transition flags $R^{+(-)} \in \{0, 1\}$ are Bernoulli random variables set by comparison to a uniform random sample $U_k \sim \mathcal{U}(0, 1)$ according to

$$R_k^{+(-)} = 1 \quad \text{if } \frac{T}{N_\Delta}\Gamma_{\text{in(out)}}(V_{g,k}) < U_k. \qquad (\text{C2})$$

Here, $V_{g,k}$ includes both the harmonic resonator response due to the excitation signal and the response $V_g(t)$ due to the tunneling events in the SEB (steps in $Q(t)$), represented by the convolution in Eq. (30). The relevant transfer functions can be derived from simple circuit theory, using the values defined in the main text, as

$$H_{QG}(s) = \frac{V_g(s)}{Q(s)} = \frac{\alpha s^2 L(1 + sC_cZ_0)}{B + s^2 C_c L},$$

$$H_{QB}(s) = \frac{V_b(s)}{Q(s)} = \frac{\alpha Z_0 s^3 LC_c}{B + s^2 C_c L},$$

$$H_{FG}(s) = \frac{V_g(s)}{V_f(s)} = \frac{2}{1 + (sC_r + G_r + 1/sL)(1/sC_c + Z_0)},$$

$$H_{FB}(s) = \frac{V_b(s)}{V_f(s)} = \frac{1 + (sC_r + G_r + 1/sL)(1/sC_c - Z_0)}{1 + (sC_r + G_r + 1/sL)(1/sC_c + Z_0)},$$
$$(\text{C3})$$

where $B = (1 + sC_cZ_0)(1 + sLG_r + s^2(C_r + \alpha C_S)L)$. As $Q(t)$ is composed only of steps, the convolution can be implemented exactly by an infinite impulse-response (IIR) discrete-time filter with coefficients calculated by a step-invariant transformation of the continuous-time resonator transfer function:

$$H_{\text{IIR}}(z) = \left(\frac{z-1}{z}\right)\mathcal{Z}\left(\mathcal{L}^{-1}\left(\frac{H_{QG(QB)}(s)}{s}\right)_{t=kT/N_\Delta}\right). \qquad (\text{C4})$$

After sampling the inverse Laplace transform of the partial fraction expansion of $H(s)/s$ at a rate $\omega_0 N_\Delta/2\pi = N_\Delta/T$,

$$\mathcal{L}^{-1}\left(\sum_i \frac{K_i}{s + s_i}\right)_{t=kT/N_\Delta} = \sum_i K_i e^{-s_i kT/N_\Delta}, \qquad (\text{C5})$$

where $i = \{0, 1, \ldots, n_p - 1\}$ and n_p is the number of poles of $H(s)/s$, taking the Z-transform gives the set of digital filter coefficients $\{a_i\}, \{b_i\}$ according to

$$\sum_i \frac{K_i}{1 + e^{-(s_iT/N_\Delta)z^{-1}}} = \frac{\sum_i b_i z^{-i}}{\sum_i a_i z^{-i}}. \qquad (\text{C6})$$

We implement this filter in direct form II, with m being an internal state of the filter:

$$m_k = -|e|Q_k - \sum_i a_i m_{k-i}; \quad V_k = \sum_i b_i m_{k-i}. \qquad (\text{C7})$$

Synchronous demodulation is modeled numerically by down-mixing $V_d(t) = V_b(t) \times \sqrt{2}\cos(\omega_c t + \varphi)$ followed by a digital low-pass filter (fifth-order Butterworth with cutoff frequency $\omega_0/10$). The sampling rate of the output $V_X(t)$ is then decimated from $N_\Delta\omega_0/(2\pi)$ to $\omega_0/(2\pi)$, accelerating the power-spectral-density estimation without aliasing or loss of information around zero frequency, and the resonator transient response (of duration $5Q_L$ cycles, covering 99.3% of the transient decay) is cropped.

We estimate the zero-frequency noise-power spectrum $S_X(0)$ from a fast Fourier transform (FFT) based periodogram calculation, taking the component at the lowest nonzero frequency ω_0/N_{cyc}, where N_{cyc} is the duration of the simulation, with the standard error calculated from the variance of N trials. Simulations demodulated at different local oscillator phases θ are fitted to the trochoid function $S_X(\varphi) = S_X^0 + \Delta S_X \cos(2\varphi + \theta)$ [as introduced in the main text; see also Fig. 5(e)] gives the final estimates of the cyclostationary spectral correlation densities S_X and ΔS_X, with errors calculated from the covariances of the fitting parameters.

In the case of the current-noise spectral correlation functions $S_I^{n\omega_0}(\omega)$, the estimate is derived directly from the time
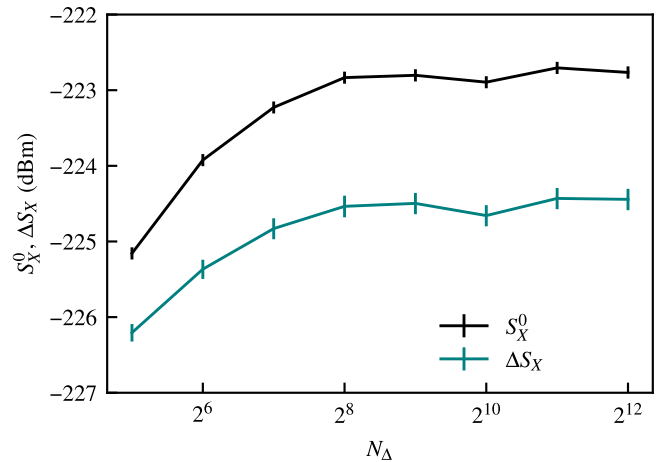

FIG. 6. The convergence of the simulated spectral correlation densities with N_Δ.

series $Q(t)$ using the relation [32]:

$$R_N^{n\omega_0}(\tau) = \int_{-\infty}^{\infty} N(t)N(t+\tau)e^{jn\omega_0 t}\, dt \qquad \text{(C8)}$$

in conjunction with Eq. (12).

We pick the simulation time step by assessing the convergence of the extracted spectral correlation densities with increasing N_Δ as shown in Fig. 6; for 500 trials of duration $N_{\text{cyc}} = 2^{14}$, the values converge to within the standard error by $N_\Delta = 2^{11}$.

---

[1] A. Chatterjee, P. Stevenson, S. De Franceschi, A. Morello, N. P. de Leon, and F. Kuemmeth, Semiconductor qubits in practice, Nat. Rev. Phys. **3**, 157 (2021).

[2] R. Maurand, X. Jehl, D. Kotekar-Patil, A. Corna, H. Bohuslavskyi, R. Laviéville, L. Hutin, S. Barraud, M. Vinet, M. Sanquer, and S. De Franceschi, A CMOS silicon spin qubit, Nat. Commun. **7**, 13575 (2016).

[3] A. M. J. Zwerver, *et al.*, Qubits made by advanced semiconductor manufacturing, Nat. Electron. **5**, 184 (2022).

[4] A. Ruffino, T.-Y. Yang, J. Michniewicz, Y. Peng, E. Charbon, and M. F. Gonzalez-Zalba, A cryo-CMOS chip that integrates silicon quantum dots and multiplexed dispersive readout electronics, Nat. Electron. **5**, 53 (2022).

[5] S. G. J. Philips, M. T. Mądzik, S. V. Amitonov, S. L. de Snoo, M. Russ, N. Kalhor, C. Volk, W. I. L. Lawrie, D. Brousse, L. Tryputen, B. P. Wuetz, A. Sammak, M. Veldhorst, G. Scappucci, and L. M. K. Vandersypen, Universal control of a six-qubit quantum processor in silicon, Nature **609**, 919 (2022).

[6] X. Xue, M. Russ, N. Samkharadze, B. Undseth, A. Sammak, G. Scappucci, and L. M. K. Vandersypen, Quantum logic with spin qubits crossing the surface code threshold, Nature **601**, 343 (2022).

[7] A. G. Fowler, M. Mariantoni, J. M. Martinis, and A. N. Cleland, Surface codes: Towards practical large-scale quantum computation, Phys. Rev. A **86**, 032324 (2012).

[8] D. V. Averin and K. K. Likharev, in *Single Charge Tunneling: Coulomb Blockade Phenomena In Nanostructures*, edited by H. Grabert and M. H. Devoret (Springer U.S., Boston, Massachusetts, 1992), p. 311.

[9] K. K. Likharev, Correlated discrete transfer of single electrons in ultrasmall tunnel junctions, IBM J. Res. Dev. **32**, 144 (1988).

[10] E. J. Connors, J. Nelson, and J. M. Nichol, Rapid high-fidelity spin-state readout in Si/Si-Ge quantum dots via rf reflectometry, Phys. Rev. Appl. **13**, 024019 (2020).

[11] R. J. Schoelkopf, P. Wahlgren, A. A. Kozhevnikov, P. Delsing, and D. E. Prober, The radio-frequency single-electron transistor (rf-SET): A fast and ultrasensitive electrometer, Science **280**, 1238 (1998).

[12] F. Vigneau, F. Fedele, A. Chatterjee, D. Reilly, F. Kuemmeth, M. F. Gonzalez-Zalba, E. Laird, and N. Ares, Probing quantum devices with radio-frequency reflectometry, Appl. Phys. Rev. **10**, 021305 (2023).

[13] M. G. House, I. Bartlett, P. Pakkiam, M. Koch, E. Peretz, J. van der Heijden, T. Kobayashi, S. Rogge, and M. Y. Simmons, High-sensitivity charge detection with a single-lead quantum dot for scalable quantum computation, Phys. Rev. Appl. **6**, 044016 (2016).

[14] F. Borjans, X. Mi, and J. Petta, Spin digitizer for high-fidelity readout of a cavity-coupled silicon triple quantum dot, Phys. Rev. Appl. **15**, 044052 (2021).

[15] D. J. Niegemann, V. El-Homsy, B. Jadot, M. Nurizzo, B. Cardoso-Paz, E. Chanrion, M. Dartiailh, B. Klemt, V. Thiney, C. Bäuerle, P.-A. Mortemousque, B. Bertrand, H. Niebojewski, M. Vinet, F. Balestro, T. Meunier, and M. Urdampilleta, Parity and singlet-triplet high-fidelity readout in a silicon double quantum dot at 0.5 K, PRX Quantum **3**, 040335 (2022).

[16] G. A. Oakes, *et al.*, Fast high-fidelity single-shot readout of spins in silicon using a single-electron box, Phys. Rev. X **13**, 011023 (2023).

[17] A. N. Korotkov, Intrinsic noise of the single-electron transistor, Phys. Rev. B **49**, 10381 (1994).

[18] M. Amman, K. Mullen, and E. Ben-Jacob, The charge-effect transistor, J. Appl. Phys. **65**, 339 (1989).

[19] S. Kafanov and P. Delsing, Measurement of the shot noise in a single-electron transistor, Phys. Rev. B **80**, 155320 (2009).

[20] A. N. Korotkov and M. A. Paalanen, Charge sensitivity of radio frequency single-electron transistor, Appl. Phys. Lett. **74**, 4052 (1999).

[21] L. Roschier, P. Hakonen, K. Bladh, P. Delsing, K. W. Lehnert, L. Spietz, and R. J. Schoelkopf, Noise performance of the radio-frequency single-electron transistor, J. Appl. Phys. **95**, 1274 (2004).

[22] M. H. Devoret and R. J. Schoelkopf, Amplifying quantum signals with the single-electron transistor, Nature **406**, 1039 (2000).

[23] A. Aassime, G. Johansson, G. Wendin, R. J. Schoelkopf, and P. Delsing, Radio-frequency single-electron transistor as readout device for qubits: Charge sensitivity and backaction, Phys. Rev. Lett. **86**, 3376 (2001).

[24] D. Keith, M. G. House, M. B. Donnelly, T. F. Watson, B. Weber, and M. Y. Simmons, Single-shot spin readout in semiconductors near the shot-noise sensitivity limit, Phys. Rev. X **9**, 041003 (2019).

[25] D. V. Averin and J. P. Pekola, Statistics of the dissipated energy in driven single-electron transitions, Europhys. Lett. **96**, 67004 (2011).

[26] J. P. Pekola, Towards quantum thermodynamics in electronic circuits, Nat. Phys. **11**, 118 (2015).

[27] J. V. Koski, V. F. Maisi, J. P. Pekola, and D. V. Averin, Experimental realization of a Szilard engine with a single electron, Proc. Natl. Acad. Sci. **111**, 13786 (2014).

[28] M. Albert, C. Flindt, and M. Büttiker, Accuracy of the quantum capacitor as a single-electron source, Phys. Rev. B **82**, 041407 (2010).

[29] A. Mahé, F. D. Parmentier, E. Bocquillon, J.-M. Berroir, D. C. Glattli, T. Kontos, B. Plaçais, G. Fève, A. Cavanna, and Y. Jin, Current correlations of an on-demand single-electron emitter, Phys. Rev. B **82**, 201309 (2010).

[30] F. D. Parmentier, E. Bocquillon, J.-M. Berroir, D. C. Glattli, B. Plaçais, G. Fève, M. Albert, C. Flindt, and M. Büttiker,

Current noise spectrum of a single-particle emitter: Theory and experiment, Phys. Rev. B **85**, 165438 (2012).

[31] T. Jonckheere, T. Stoll, J. Rech, and T. Martin, Real-time simulation of finite-frequency noise from a single-electron emitter, Phys. Rev. B **85**, 045321 (2012).

[32] W. A. Gardner, A. Napolitano, and L. Paura, Cyclostationarity: Half a century of research, Signal Process. **86**, 639 (2006).

[33] N. Dittmann and J. Splettstoesser, Finite-frequency noise of interacting single-electron emitters: Spectroscopy with higher noise harmonics, Phys. Rev. B **98**, 115414 (2018).

[34] M. Moskalets, Noise of a single-electron emitter, Phys. Rev. B **88**, 035433 (2013).

[35] M. F. Gonzalez-Zalba, S. Barraud, A. J. Ferguson, and A. C. Betz, Probing the limits of gate-based charge sensing, Nat. Commun. **6**, 6084 (2015).

[36] K. D. Petersson, C. G. Smith, D. Anderson, P. Atkinson, G. A. C. Jones, and D. A. Ritchie, Charge and spin state readout of a double quantum dot coupled to a resonator, Nano Lett. **10**, 2789 (2010).

[37] J. M. Elzerman, R. Hanson, L. H. Willems van Beveren, B. Witkamp, L. M. K. Vandersypen, and L. P. Kouwenhoven, Single-shot read-out of an individual electron spin in a quantum dot, Nature **430**, 431 (2004).

[38] W. A. Gardner, A unifying view of coherence in signal processing, Signal Process. **29**, 113 (1992).

[39] F.-E. Von Horstig, D. J. Ibberson, G. A. Oakes, L. Cochrane, D. F. Wise, N. Stelmashenko, S. Barraud, J. A. Robinson, F. Martins, and M. F. Gonzalez-Zalba, Multi-module microwave assembly for fast readout and charge-noise characterization of silicon quantum dots, Phys. Rev. Appl. **21**, 044016 (2024).

[40] V. Derakhshan Maman, M. Gonzalez-Zalba, and A. Pályi, Charge noise and overdrive errors in dispersive readout of charge, spin, and Majorana qubits, Phys. Rev. Appl. **14**, 064024 (2020).

[41] G. Oakes, L. Peri, L. Cochrane, F. Martins, L. Hutin, B. Bertrand, M. Vinet, A. Gomez Saiz, C. Ford, C. Smith, and M. Gonzalez-Zalba, Quantum dot-based frequency multiplier, PRX Quantum **4**, 020346 (2023).

[42] D. J. Ibberson, T. Lundberg, J. A. Haigh, L. Hutin, B. Bertrand, S. Barraud, C.-M. Lee, N. A. Stelmashenko, G. A. Oakes, L. Cochrane, J. W. Robinson, M. Vinet, M. F. Gonzalez-Zalba, and L. A. Ibberson, Large dispersive interaction between a CMOS double quantum dot and microwave photons, PRX Quantum **2**, 020315 (2021).

[43] J. Schleeh, G. Alestig, J. Halonen, A. Malmros, B. Nilsson, P. A. Nilsson, J. P. Starski, N. Wadefalk, H. Zirath, and J. Grahn, Ultralow-power cryogenic InP HEMT with minimum noise temperature of 1 K at 6 GHz, IEEE Electron Device Lett. **33**, 664 (2012).

[44] S. Schaal, I. Ahmed, J. A. Haigh, L. Hutin, B. Bertrand, S. Barraud, M. Vinet, C.-M. Lee, N. Stelmashenko, J. W. A. Robinson, J. Y. Qiu, S. Hacohen-Gourgy, I. Siddiqi, M. F. Gonzalez-Zalba, and J. J. L. Morton, Fast gate-based readout of silicon quantum dots using Josephson parametric amplification, Phys. Rev. Lett. **124**, 067701 (2020).

[45] M. Mück and R. McDermott, Radio-frequency amplifiers based on dc SQUIDs, Supercond. Sci. Technol. **23**, 093001 (2010).